Journal of Innovative Image Processing (ISSN: 2582-4252)
www.irojournals.com/iroiip/

Adaptive Lung Segmentation Using Optimal U-Net and Grey Wolf Optimization for COVID-19 Chest X-Rays

Anitha Patibandla[1], Manu Prakram[2]

Department of Electronics and Electrical Engineering, Lovely Professional University, Punjab, India.

E-mail: [1]anithakamal.ghanta@gmail.com, [2]manu.14704@lpu.co.in

Abstract

The chest X-ray imaging (CXR) is a key diagnostic instrument in COVID-19 diagnosis, wherein more than 600,000 tests are performed worldwide annually and the misdiagnosis rate is estimated to be 15-20 percent, largely contributed by human error. Conventional manual reading of CXR images is time-consuming, labor-intensive, and heavily reliant on the skill of the radiologist, typically resulting in a series of uneven and sluggish diagnostic outcomes. To overcome these limitations, the current research introduces an innovative state-of-the-art CXR segmentation model based on rigorous preprocessing techniques in combination with the optimisation of deep-learning algorithms to obtain precise lung parenchyma and pathological lesion outlines. Block-matching 3D filtering (BM3D) was applied to suppress noise without loss of anatomical details following curation of the COVID-19 CXR Dataset. The Optimization U-Net (OU-Net) architecture, which served as the backbone of the proposed approach, was carefully designed with adaptive encoder-decoder paths and strengthened skip connections to better subdivide real lung regions and manifestations of diseases. Additionally, the training schedule utilizes Modified Grey Wolf Optimization (MGWO) for the optimization of network parameters, and this accelerates convergence and enhances segmentation accuracy. Empirical results confirm that the OU-Net with MGWO is superior to conventional and standard deep-learning models, as the suggested approach enhances accuracy by 4.58%, sensitivity by 5.22%, specificity by 4.60%, precision by 4.85%, recall by 1.78%, F1-score by 5.07%, Jaccard index by 5.23%, and Dice score by 5.31%.

Keywords: Block-matching and 3D Filtering, COVID-19, Chest X-Ray, Grey Wolf Optimization, Optimal U-Net, Segmentation.

1. Introduction

Over 777 million confirmed COVID-19 cases and 7.1 million deaths were reported globally by mid-May 2025, translating to a global fatality rate of about 0.91% of confirmed infections [1]. Although many studies indicate much higher excess mortality, perhaps more than twice the reported amount, these figures represent the official counts [2]. Although some resurgence has been observed in parts of Asia and the Middle East, test positivity rates and reported new cases have decreased in recent months in many regions [3]. It is essential to accurately segment the lung regions in CXRs to identify abnormalities related to COVID-19, such as consolidations and ground-glass opacities [4]. Segmentation enables Artificial

DOI: https://doi.org/10.36548/jiip.2025.4.010
Received: 05.09.2025, received in revised form: 03.10.2025, accepted: 16.10.2025, published: 29.10.2025

Intelligence (AI) models to focus on areas that signal infection, by isolating the relevant pulmonary structures and addressing artifacts caused by confounding anatomical structures. This technique of refining methodology results in an effective and dependable process of analysis in the event of an epidemic surge, when swift triage and diagnosis can significantly affect patient outcomes [5].

Several companies have increased the creation of AI programs to analyze chest images to support the diagnosis of COVID-19. RADLogics has deployed a Deep Learning (DL) application that generates a disease-severity score (also known as the Corona score) for CT and CXR scans in Chinese, Russian, and Italian hospitals [6]. The DAMO Academy of Alibaba presented an AI model, which provides a diagnosis within 20 seconds with an accuracy of 96 percent in 26 Chinese hospitals. The system has already been implemented, and has processed more than 30,000 cases [7]. South Korean based Lunit has also made its AI-assisted CXR analysis software available free of charge, facilitating triage activities at COVID-19 centers in South Korea and implementing the technology in one of the largest hospital systems in Brazil [8].

Various hospital chains have embraced the use of AI to enhance the screening and flow of patients. The Zhongnan Hospital in Wuhan used an AI system created by InferVision that was trained on thousands of cases of COVID- [9] and utilized across 34 hospitals that scanned over 32,000 patients to quickly prioritize potentially infected patients. South Australian Medical Imaging employed the Annalise.ai AI technology in six metropolitan and four regional hospitals in South Australia [10]. The system identifies areas of interest in CXRs in a similar way a spell-checker works thus allowing radiologist to be fast and accurate without adding extra costs to patients. The novel contributions of the work are as follows:

- To integrate BM3D preprocessing with DL segmentation, effectively reducing noise while preserving fine lung and lesion structures of COVID-19.
- To develop an OU-Net architecture with adaptive encoder-decoder layers and attention-guided skip connections, enhancing segmentation of both normal and pathological COVID-19 regions.
- To employ MGWO for automatic tuning of OU-Net hyperparameters, improving convergence speed and segmentation accuracy beyond standard optimization techniques.

This paper is structured into five key sections: Section 2 provides a comprehensive survey of existing studies, Section 3 details the proposed methodology with BM3D preprocessing, OU-Net segmentation, and MGWO optimization, Section 4 presents experimental results with detailed discussions, and Section 5 concludes with key findings and future research directions.

2. Related Work

Bahroun [11] suggested a two-step Convolutional Auto-Encoder (CAE) model, which did not process images altogether but rather the segmented CT scans and CXR images independently and then combined the features obtained to identify COVID-19. The framework, nevertheless, made the computation more complex with dual path features processing. Orenc [12] introduced a better segmentation method that utilized several variants of U-Net and Ant

Colony Optimization (ACO) to optimize the encoder-decoder-based architectures and consequently generated fine-grained lung contours in CXR images. This approach, however, was incapable of maintaining strength with highly unbalanced data. Gtifa [13] presented a Cuckoo Search Optimized (CSO) multi-level thresholding scheme together with a Convolutional Neural Network (CNN), which optimized feature capture of CXR images to identify COVID-19 and associated lung diseases. Multi-level thresholding, on the other hand, was computationally appropriate but not as scalable to large datasets.

Vinothini [14] suggested a more developed framework for segmentation and severity-prediction, which used nnU-Net to extract lung regions and a faster region-based CNN with a gated joint selection algorithm to grade the severity. Mehta [15] proposed a MultiResUNet-based DL model that can learn the multi-scale contextual features of the image to accurately segment the lungs in the CXR dataset, but their performance degraded when using CXRs with low contrast or high noise. Herng [16] suggested a segmentation scheme with variant k-means clustering algorithms, which segmented CXR images into optimal clusters to improve the localization of COVID19 lesions; the clustering scheme was sensitive to centroid selection, thus affecting stability.

Kang [17] suggested a segmentation-aided fusion-based classification algorithm and used a combination of segmented CXR images and a complementary feature fusion to automatically analyse the image; however, high-quality segmentation masks were necessary, and the errors during the segmentation process were transferred to the analysis results. Din [18] introduced a DL network called CXR-Seg, which used a modified Deep Auto Encoder (DAE) optimised by the Whale Optimization Algorithm (WOA) to learn precise lung boundaries using CXR datasets, but the model required a large amount of labeled training data, which cannot be used in scenarios with scarce data. Biju [19] developed a DL-based segmentation method that identified infected lung areas of the CXR scan before subjecting the image to a classification process, which was less accurate when lesions blended with normal body features.

Kumari [20] proposed an Optimised K-Means Clustering (OKMC) segmentation model with a hybrid Visual Geometry Group (VGG19) Support Vector Machine (SVM) model to classify COVID-19. The k-means algorithm was used to divide the infected lung areas, and VGG19 was used to extract the features that were then classified using SVM, however, there was a drop in segmentation accuracy when there was low contrast and uneven intensity distribution in the images. Otair [21] suggested a locally adaptive thresholding algorithm, which optimally adjusted the threshold values to partition the inflicted lung areas of CXR images by COVID-19; the algorithm was not very robust to high inter-patient differences in lung textures. Slika [22] suggested a parallel framework based on Vision Mamba (VMamba) and Dragonfly Optimisation Attention (DAA) that combined lung segmentation and replacement augmentation to predict pneumonia severity using CXR; the parallel framework added complexity to the architecture, which made the minimisation of deployment challenging.

Qi [23] proposed AO-TransUNet, a multi-attention optimization network that extended the conventional U-Net architecture with transformer-based modules. However, the transformer integration required high computational resources, limiting real-time applicability. Alaoui Abdalaoui Slimani [24] proposed an enhanced U-Net++ model that integrated discrete wavelet transforms with attention gate mechanisms for pathological lung segmentation in CXR. However, the model showed performance degradation on noisy datasets due to over-sensitivity in feature selection. Su [25] proposed COVSeg-VLM, a vision–language model that aligned textual prompts with visual CXR features to segment COVID-19 infections. However, the reliance on prompt engineering reduced consistency across diverse clinical settings.

3. Proposed Work

The algorithm described below includes a new synthesis of pre-processing, DL segmentation, and meta-heuristic optimization, specifically set up for COVID-19 CXR images. Figure 1 demonstrates the proposed system architecture. Finally, an OUNet with MGWO is utilized to automatically tune hyperparameters such as the learning rate, convolutional filter sizes, and batch normalization parameters, hence guaranteeing rapid convergence and high Dice coefficients. The combination of BM3D, OU-Net, and MGWO in a unified CXR segmentation process is a contribution that has yet to be mentioned in the existing literature.

Step 1: BM3D Preprocessing: BM3D filters were applied to each CXR image to remove noise without distorting the coarse anatomy of the pulmonary fields. This preprocessing step ensures that salient features required in the segmentation process are retained and improves further feature extraction.

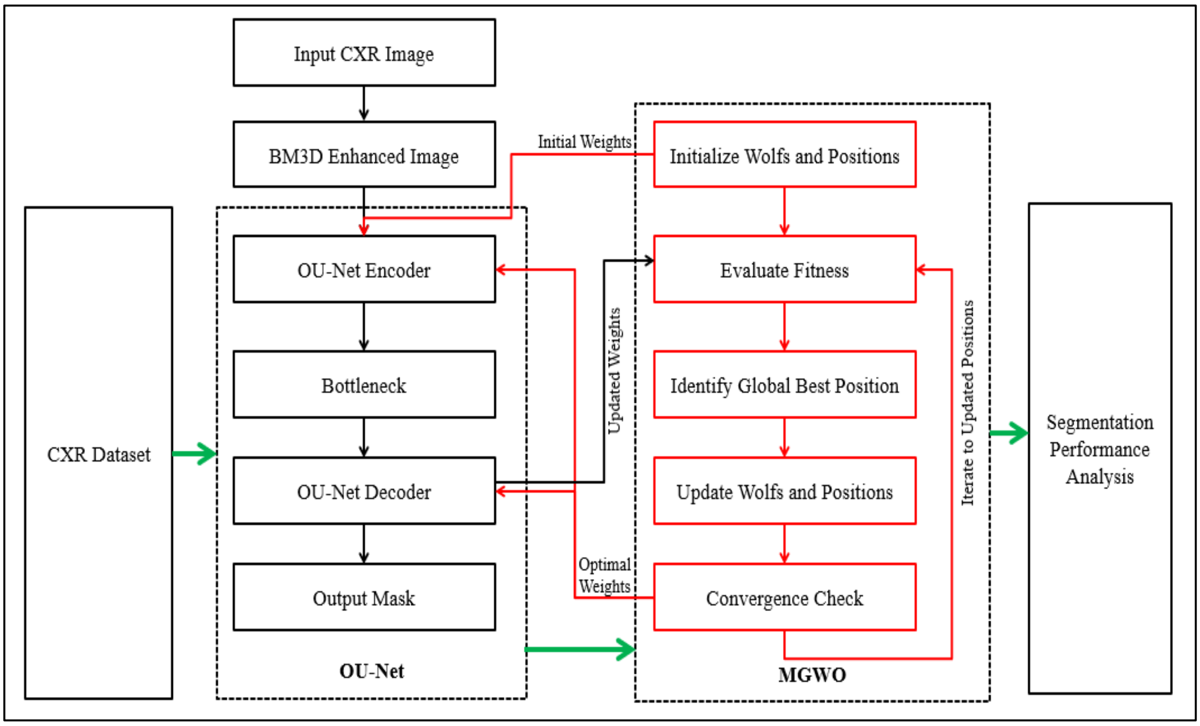

Figure 1. Proposed System Architecture

Step 2: OU-Net Segmentation: Images processed by BM3D were used to train the OU-Net architecture. Its encoder-decoder architecture uses adjustable layers and attention-based skip-connections that highlight the important areas. Dynamic feature weighting is applied to ensure that the network can pay attention to both the lung boundaries and the pathological structures therefore performing better in segmentation.

Step 3: MGWO: The OU-Net hyper-parameters including convolutional kernel sizes, learning rate and dropout rates were optimised using the MGWO algorithm. Using the hierarchical hunting behavior exhibited by grey wolves, MGWO exploits the parameter space more efficiently, with faster convergence as well as improved segmentation performance.

Step 4: Segmentation Evaluation: The completed segmented images were assessed in terms of metrics such as the dice coefficient, sensitivity, and global accuracy. The comparison with traditional DL algorithms demonstrates the high performance of the OU-Net +MGWO method in performing automated and accurate segmentation of COVID-19.

3.1 OU-Net Segmentation

The OU-Net model is suggested with several structural changes compared to the traditional U-Net and the Attention U-Net, which are intended to strengthen the refinement of features and preserve spatial integrity when identifying infection regions in the lungs. OU-Net uses optimised up-sampling units with adaptive skip pathways that filter and fuse adaptive features to optimise redundant activations, unlike the regular U-Net which uses direct skip connections between encoder and decoder layers. Although maintaining the encoder-decoder depth of the Attention-U-Net, OU-Net uses hybrid convolutional blocks with channel recalibration modules, which do not require all-is-well encodings in channel recalibrations, as a result, they do not have this attribute offered.

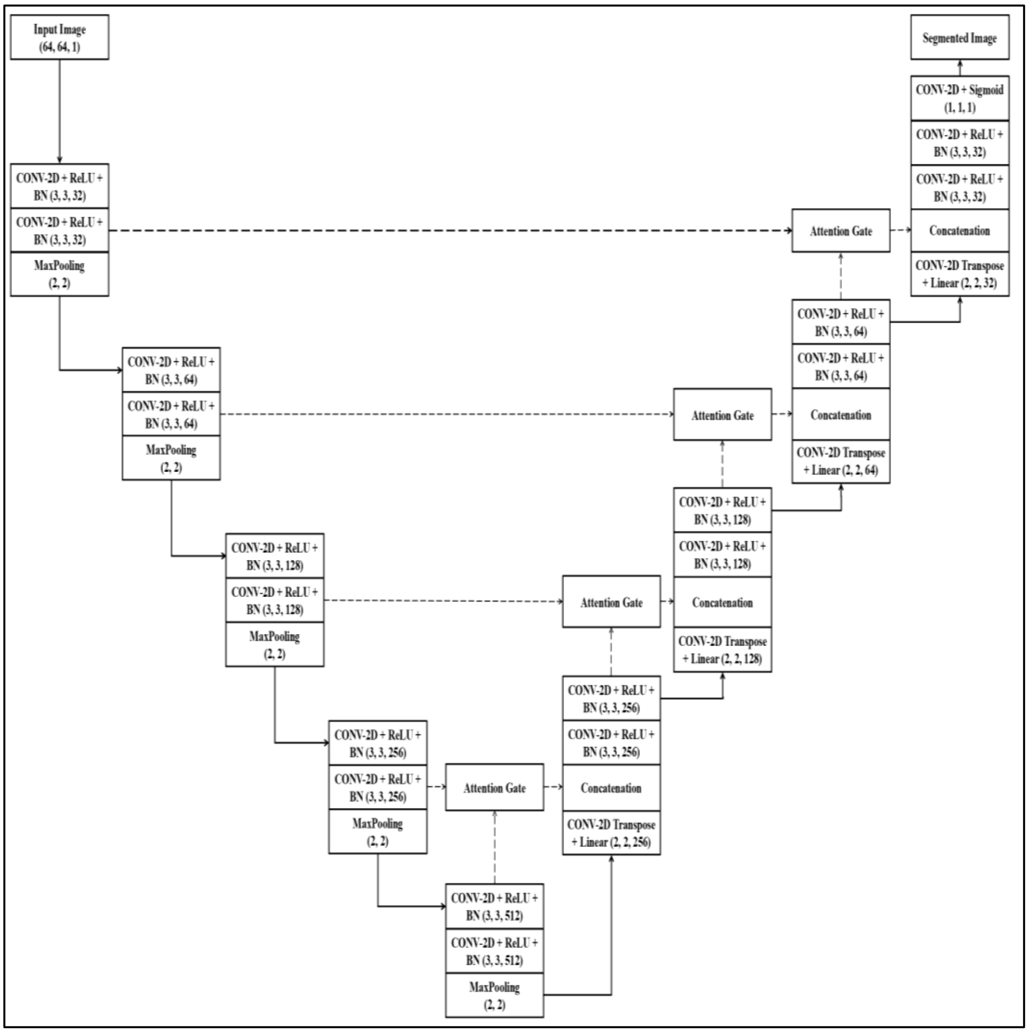

Figure 2. Proposed OU-Net System Architecture

Figure 2 above is an optimised extension of the traditional U-Net model specifically designed to extract lung regions in COVID-19 patient CXR images introduced as the OU-Net segmentation model. It operates on an encoder-decoder design where hierarchical feature representations are extracted using the encoder, but their output is rebuilt accordingly to form spatial details to accurately outline lung boundaries using the decoder. Unlike the regular U-Net, OU-Net also includes attention to refined convolutional blocks and optimized skip connections to maintain contextual information as well as increase the level of precision at the boundary. This design allows the model to resolve fine differences in the infected lung tissues, and it can cope with problems caused by low contrast and overlapping anatomies. Therefore, OU -Net provides credible segmentation of lung areas, which constitutes a foundational stage for downstream activities like detecting infections, assessing the disease, and automated diagnosis of COVID -19.

The proposed OU-Net algorithm is provided in Table1. First, the notation of $F^{l}_{i,j,k}$ is used to refer to the feature map in the layer l at the position (i,j) and channel (k). The convolutional filter weights, denoted by $W^{l}_{m,n,c,k}$ represent the input data of the input channel c and j output channel k and b^{l}_{k} is the bias (the bias unit is left out). This is an operation that retrieves local patterns in the input feature maps.

$$F^{l}_{i,j,k} = \sum_{m=1}^{M} \sum_{n=1}^{N} \sum_{c=1}^{C} W^{l}_{m,n,c,k} . X^{l-1}_{i+m,j+n,c} + b^{l}_{k} \tag{1}$$

In this case, $A^{l}_{i,j,k}$ is a feature map that is activated at the dispensation of the used layers (l) and it is the result of applying the Rectified Linear Unit (ReLU) to the $F^{l}_{i,j,k}$. The ReLU adds non-linearity, and therefore, allows the network to acquire complicated patterns.

$$A^{l}_{i,j,k} = \max\left(0, F^{l}_{i,j,k}\right) \tag{2}$$

The pooled feature map $P^{l}_{i,j,k}$ was obtained with a pooling window (Ω). The pooling eliminates space dimension, conserves the dominant features and increases the efficiency of the computations.

$$P^{l}_{i,j,k} = \max_{(p,q) \in \Omega}\left(A^{l}_{i+p,j+q,k}\right) \tag{3}$$

The $U^{l}_{i,j,k}$represents the upsampled attention feature map using transposed convolution. It restores spatial resolution lost in pooling, enabling precise boundary reconstruction in segmentation.

$$U^{l}_{i,j,k} = \sum_{m=1}^{M} \sum_{n=1}^{N} W^{l}_{i,j,k,c} . P^{l-1}_{i-m,j-n,c} \tag{4}$$

Here, $S^{l}_{i,j,k}$ is the concatenated feature map combining upsampled features $U^{l}_{i,j,k}$ with the corresponding encoder features $A^{L-1}_{i,j,k}$. Skip attention connections allow retention of fine-grained spatial details.

$$S^{l}_{i,j,k} = Concat\left(U^{l}_{i,j,k}, A^{L-1}_{i,j,k}\right) \tag{5}$$

Here, $G^{l}_{i,j,k}$ is the attention map computed using weights W_g and bias b_g , with σ as the sigmoid function. It highlights relevant regions while suppressing irrelevant background features.

$$G_{i,j,k}^{l} = \sigma\left(W_g \cdot S_{i,j,k}^{l} + b_g\right) \tag{6}$$

The $SS_{i,j,k}^{l}$ is the output feature map after applying attention $G_{i,j,k}^{l}$. This enhances critical regions for accurate segmentation of lung and pathological areas.

$$SS_{i,j,k}^{l} = G_{i,j,k}^{l} . S_{i,j,k}^{l} \tag{7}$$

Here, $SS_{i,j,k}^{l}$ is the normalized feature map, where μ_k and σ_k^2 are the mean and variance of channel k, γ_k and β_k are learnable scaling and shift parameters, and ϵ is a small constant. Batch normalization stabilizes training and accelerates convergence.

$$SS_{i,j,k}^{l} = \frac{SS_{i,j,k}^{l} - \mu_k}{\sqrt{\sigma} + \epsilon} . \gamma_k + \beta_k \tag{8}$$

The $Y_{i,j,c}$ is the predicted probability that pixel (i,j) belongs to class c. Sigmoid ensures class probabilities sum to 1, providing multi-class segmentation outputs.

$$Y_{i,j,c} = \frac{e^{SS_{i,j,k}^{l}}}{\sum e^{SS_{i,j,k}^{l}}} \tag{9}$$

Table 1. Proposed OU-Net Algorithm

Convolution Layer: Extract local patterns from input feature maps using convolutional filters and biases (Eq. 1)
Activation: Apply the Rectified Linear Unit to introduce non-linearity and retain positive activations (Eq. 2).
Pooling: Perform max pooling over a window to reduce spatial dimensions while preserving dominant features (Eq. 3).
Upsampling: Restore spatial resolution in the decoder using transposed convolution to recover fine details (Eq. 4).
Skip attention concatenation: Concatenate upsampled decoder features with corresponding encoder features through skip connections to retain fine-grained information (Eq. 5).
Attention map generation: Compute attention weights that highlight relevant lung regions and suppress background noise (Eq. 6).
Attention-based refinement: Refine concatenated features by applying the attention map to emphasize critical segmentation regions (Eq. 7).
Normalization: Normalize feature maps with batch normalization (learnable scale and shift) to stabilize and accelerate training (Eq. 8).
Segmentation Mask: Convert final feature responses to per-pixel class probabilities via the sigmoid formulation for segmentation (Eq. 9).
Loss minimization: Optimize network parameters by minimizing Dice loss (evaluated with MGWO) to maximize overlap with ground truth masks (Eq. 10).

Here, L_{dice} measured by MGWO with similarity between predicted mask Y_{ij} and ground truth G_{ij}, with ϵ preventing division by zero. Minimizing Dice loss ensures accurate overlap of segmented regions.

$$L_{dice} = 1 - \frac{2\sum Y_{ij},G_{ij}}{\sum Y_{ij}+\sum G_{ij}+\epsilon} \tag{10}$$

3.2 MGWO Loss Optimization

The MGWO loss optimization worked as a powerful strategy to refine lung region extraction from CXR images of COVID-19 patients. Figure 3 shows the proposed MGWO loss optimization flowchart. Inspired by the natural hunting and leadership hierarchy of grey wolves, MGWO adapted the positions of candidate solutions to minimize segmentation errors during model training. In this process, the best-performing solutions acted like alpha, beta, and delta wolves guiding the search, while the others explored around them to find more accurate boundaries. By embedding this mechanism into the loss optimization stage, MGWO helped the segmentation network focus on reducing false predictions and enhancing boundary accuracy. With these mechanisms, the extracted lung regions are not only accurate, but also resistant to noise, low contrasts, and irregular patterns of infection and, eventually, add to the credibility of automated diagnosis of COVID-19. The pseudocode of the MGWO suggest algorithm is provided in Table 2. First, X_i denotes the location of the i-th wolf in a D dimensional search space and N refers to the count of wolves. Every posture defines a space of the OU-Net hyperparameters (learning rate, kernel size, dropout, and so on) to optimise.

$$X_i = [x_{i1}, x_{i2}, \ldots, x_{iD}],\ \ i = 1,2,\ldots,N \tag{11}$$

The flow of the MGWO model is characterized by the following fitness function, which uses a set of hyperparameters and the segmentation loss of the OU-Net as an indicator of how well the model recovers its ground-truth lung region. Informally, the fitness of each wolf position, denoted as X_i, representing a candidate set of hyperparameters is evaluated as follows:

$$f(X_i) = L(X_i) \tag{12}$$

In this case, $L(X_i)$ is normally Dice Loss or Cross-Entropy Loss. A smaller value of $f(X_i)$ provides an optimum solution i.e. the OU-Net segmentation based on those hyperparameters has the lowest number of errors. This expression leads MGWO to hyperparameter combinations that optimise accuracy and boundary precision of segmentation and reduce the false predictions. The alpha (X_α), beta (X_β), and delta (X_δ) are considered as the best, second and third wolves respectively. They coordinate the rest of the wolves in the process of optimizing, and convergence to optimal solutions is assured.

$$X_\alpha = best\big(f(X)\big) \tag{13}$$

$$X_\beta = second_{best(f(X))} \tag{14}$$

$$X_\delta = third\_best\big(f(X)\big) \tag{15}$$

Then, D represents the distance between the present position of a wolf, $X\ (t\ )$, and a prey, X_p, scaled by a constant C. This distance determines the strength of attraction to leaders.

$$D = \mid C \cdot X_p - X(t) \mid \tag{16}$$

Every wolf model its position depending on alpha, beta and delta wolves. The coefficients A and D are dynamic, regulating step size and direction, which balances exploration and exploitation around leaders.

$$X_1 = X_\alpha - A_1 \cdot D_\alpha \tag{17}$$

$$X_2 = X_\beta - A_2 \cdot D_\beta \tag{18}$$

$$X_3 = X_\delta - A_3 \cdot D_\delta \tag{19}$$

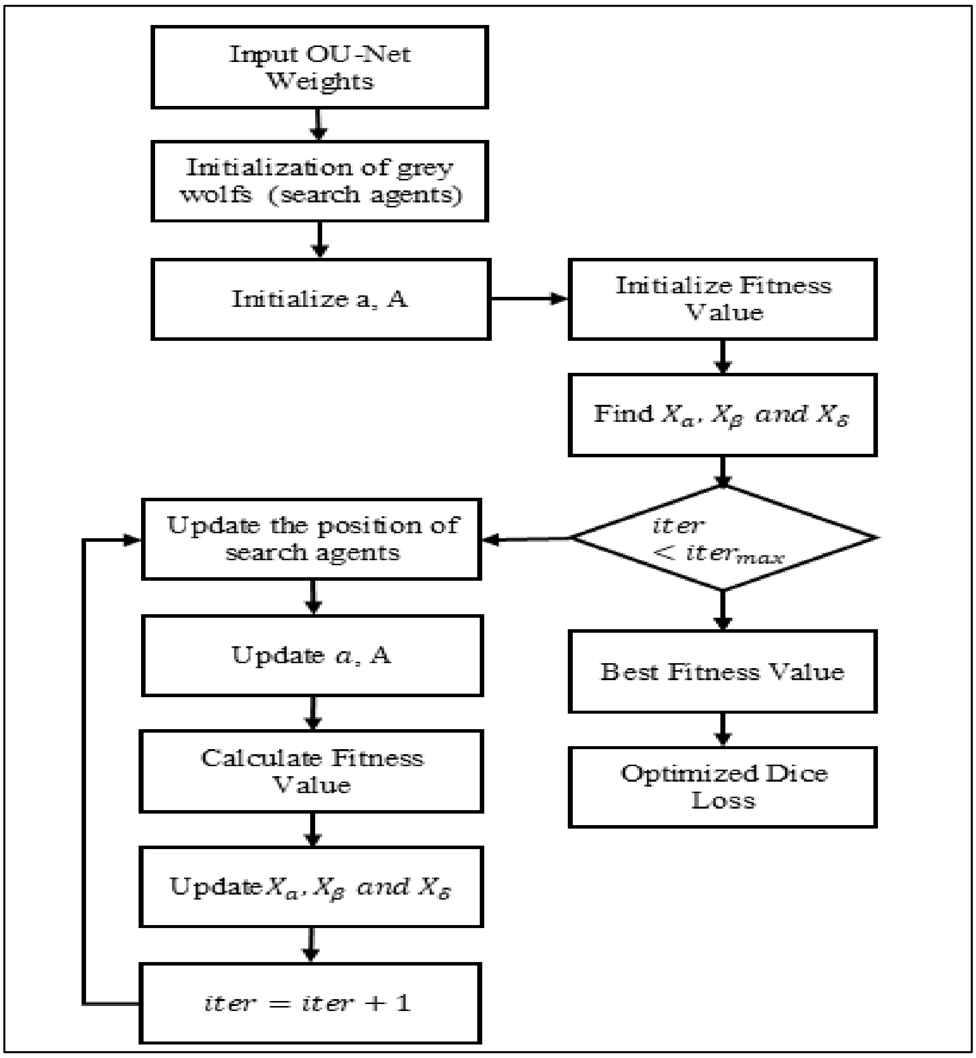

Figure 3. Proposed MGWO Flowchart

The new position of a wolf (X_{new}) is the weighted average of the positions of a wolf with respect to alpha, beta and delta wolves. This consensus mechanism will have strong movement to the global optimum and not the local minima.

$$X_{new} = X_1 + X_2 + X_3 \tag{20}$$

Coefficient A controls exploration and exploitation, where a decreases linearly over iterations t out of total T. Random vector $r \in [0,1]$ adds stochastic behavior to avoid premature convergence.

$$A = 2a \cdot r - a \tag{21}$$

$$a = 2 - \frac{2t}{T} \tag{22}$$

Table 2. Proposed MGWO Loss Optimization Pseudo Code

Inputs: D ← Dimension of search space (number of hyperparameters) N ← Number of wolves (population size) T ← Maximum iterations ε ← Convergence threshold $L(X)$ ← Loss function (Dice or Cross-Entropy) η ← Adaptive learning rate for gradient refinement **Output:** X_{alpha} ← Optimized OU-Net hyperparameters)
Step 1. Initialize population of N wolves: For each wolf $i = 1\ to\ N$: $X_i = [x_{i1}, x_{i2}, \dots, x_{iD}]$ // Random initialization in D-dimensional hyperparameter space **Step 2.** Evaluate fitness of each wolf: For each wolf $i = 1\ to\ N$: $f(X_i) = L(X_i)$ **Step 3.** Identify leadership hierarchy: Estimate X_α, X_β, and X_δ using Equations (13), (14), and (15). **Step 4.** While $t < T$ and $\left\|f\left(X_{alpha}^{t+1}\right) - f\left(X_{alpha}^{t}\right)\right\| \geq \varepsilon$ do: **a.** For each wolf $i = 1\ to\ N$: Estimate D_α, D_β, and D_δ using Equation (16). // Compute distances to leaders Estimate X_1, X_2, X_3 using Equations (17), (18), and (19). // Update positions Estimate X_{new} using Equation (20). // Consensus movement Estimate $X_i^{updated}$ using Equation (24). // Gradient-based refinement **b.** Update adaptive coefficients: Linear decay (a), Exploration-exploitation control (A), Randomization factor, r ∈ [0,1] **c.** Evaluate new fitness $f\left(X_i^{updated}\right) = L\left(X_i^{updated}\right)$ **d.** Update leadership hierarchy: X_α, X_β, and X_δ as per updated fitness. **e.** Increment iteration $t = t + 1$ and stop if $\mid f\left(X_\alpha^{updated}\right) - f(X_\alpha) \mid < \epsilon$ or t=T. **Step 5.** Return X_{alpha} as the optimized hyperparameters.

The coefficient C enhances randomization in wolf movements by scaling distances with random weights. This helps maintain diversity in the population and improves global search ability in the early iterations.

$$C = 2 \cdot r \tag{23}$$

Here, $X_i^{updated}$ is the modified position update, where $\nabla L(X_{new})$ is the gradient of the loss function and η is the adaptive learning rate. This modification combines GWO with gradient descent for faster convergence.

$$X_i^{updated} = X_{new} - \eta \cdot \nabla L(X_{new}) \tag{24}$$

The algorithm stops when the improvement in alpha's fitness falls below a threshold ϵ, or when the maximum iteration count T is reached. This ensures computational efficiency while maintaining high accuracy.

$$\text{Stop if } \mid f\left(X_\alpha^{updated}\right) - f(X_\alpha) \mid < \epsilon \text{ or t=T} \tag{25}$$

4. Results and Discussion

The following section will comprise a comparative analysis of different segmentation techniques used on the same data. The analysis also highlights the performance variance through standardized measures in an effort to ensure an equitable and reliable evaluation.

4.1 Dataset

The COVID-QU-Ex dataset is a rich and multifaceted set of CXRs that reflects clinical real-world variations. The dataset was accessed via: https://www.kaggle.com/datasets/anasmohammedtahir/covidqu. It contains images obtained with varied protocols including differences in exposure time, imaging angles, and detector resolutions, thus modeling a variation in radiological equipment and conditions of operation in a variety of institutions. There are scans with high contrast and clarity as well as scans with moderate to low image quality caused by noise, motion artifacts, or uneven illumination as the imaging setups vary in their acquisition mechanisms. The information encompasses a significant range of progression of the disease, beginning with the insidious trends of early COVID-19, featuring hazy ground-glass opacities and at the extreme end, there are severe infections that have extensive consolidation and bilateral infiltrates. Also, varying patient positions (anteroposterior and posteroanterior) and anatomy further complicate the data, making it a perfect training set to design and test powerful segmentation and classification approaches. These inherent differences make the models trained on COVID-QU-Ex generalisable to a wider range of diagnostic clinical imaging conditions, which further enhances their reliability in actual diagnoses. The data consists of 10192 normal and 10 973 COVID-19 CXRs. The training set will consist of 7134 normal and 7681 COVID19 images, the validation set will also have 1529 normal and 1646 COVID19 images, and the test set will be of 1529 normal and 1646 COVID19 images without any data augmentation.

4.2 Simulation Environment

As shown in Table 3, the implemented experimental setup used Python 3.7.6 as the main programming language, accompanied by the necessary deep learning and image-processing packages, including TensorFlow 2.0.0, OpenCV, Scikit-learn, Matplotlib, and Pandas. This setup provides a solid environment for training the model and analyzing its performance. The hardware setup included a minimum of an Intel Core i5 (8th Gen) processor, 16 GB of RAM, and a 512 GB SSD, which was sufficient to support computational capability in processing CXRs as datasets and performing iterative optimization using MGWO. A 10-fold cross-validation strategy was used to ensure reliability and unbiased performance evaluation; it was segmented into ten folds, with 80 percent (train) and 20 percent (test) used within each fold to maximize generalization and minimize overfitting.

Table 3. Software and Hardware Environment with Cross-Validation

Category	Specification	Details
Software	Programming Language	Python 3.7.6
	Supporting Libraries	TensorFlow 2.0.0, OpenCV, Scikit-learn, Matplotlib, Pandas
Hardware	Processor (CPU)	Minimum: Intel Core i5 (8th Gen)
	RAM	Minimum: 16 GB
	Storage	Minimum: 512 GB SSD
Cross-Validation	Strategy	k-Fold Cross-Validation
	Number of Folds	10 folds (80% training, 20% testing per fold)

Table 4 displays the detailed comparison of the proposed MGWO and other meta-heuristic algorithms, i.e., Random Search, Standard Genetic Algorithm (GA), Particle swarm optimisation (PSO), and Standard GWO, in the optimisation of the OU-Net for lung segmentation. The initial fitness of MGWO had the highest value of 0.72 which is better than 0.65 for Random Search and 0.70 for Standard GWO and it achieved, a better best fitness of 0.9859, indicating higher convergence accuracy than GA (0.93) and PSO (0.94). It completed in fewer than 60 iterations and 25 minutes, which is considerably lower compared to Random Search (100 iterations, 45 minutes). Exploration was enhanced with the use of an adaptive nonlinear decay factor (2 to 0.2) and increased search dimensions (20) as opposed to linear decay or reduced dimensions. In MGWO, the exploration coefficient was changed dynamically to 1.0 (adaptive), making it more efficient in search. The learning rate (0.0008), batch size (32), and dropout rate (0.25) were optimised to achieve balanced performance and the spatial resolution was improved by minimising the kernel size to 3x 3. The encoder and bottleneck filters had been optimised to 48 and 192 respectively which was more efficient in parameter settings than 128 and 256 in PSO. The LeakyReLU (alpha = 0.1) activation performed better in gradient transitions than ReLU or ELU. The regularisation was moderately greater (1.5 to 0.04) to keep over-fitting in check. Computationally, MGWO consumed 8 GB of memory and 120109 FLOPs, using less memory relative to GWO (65 percent) and PSO (75 percent). The ultimate Dice loss was reduced to 0.018, indicating the presence of strong segmentation accuracy and great smoothness of the loss landscape. In addition, the ability of MGWO to smooth was very high, and its local minima avoidance was excellent compared to traditional GA and PSO, which are only moderately good in smoothing and local minima avoidance, thus making MGWO more stable in optimisation and generalisation in tasks involving the segmentation of complex medical images.

Table 4. Comparative Optimization Performance of MGWO Against Other Metaheuristic Algorithms

Parameter	Random Search	Standard GA	Standard PSO	Standard GWO	Proposed MGWO
Initial Fitness	0.65	0.67	0.68	0.70	0.72
Best Fitness Achieved	0.91	0.93	0.94	0.965	0.9859

Iterations to Convergence	100	95	85	80	60
Convergence Time (minutes)	45	42	38	35	25
Nonlinear Convergence Factor	—	Linear decay	Linear decay	Nonlinear decay (2→0)	Adaptive nonlinear decay (2→0.2)
Search Dimensions	5	8	10	15	20
Exploration Coefficient	0.8	0.85	0.9	0.9	1.0 (adaptive)
Learning Rate	1e-4	3e-4	5e-4	6e-4	0.0008
Batch Size	64	64	64	48	32
Number of Filters (Base Encoder)	64	96	128	96	48 (optimized)
Number of Filters (Bottleneck Layer)	128	192	256	224	192
Dropout Rate	0.65	0.55	0.45	0.35	0.25
Kernel Size	7×7	5×5	7×7	5×5	3×3
Activation Function	ELU	ReLU	ReLU	ReLU	LeakyReLU (α = 0.1)
Regularization Coefficient	1e-5	5e-5	1e-4	1.2×10^{-4}	1.5×10^{-4}
Memory Usage (GB)	14	13	12	11	8
FLOPs ($\times10^{9}$)	150	165	175	150	120
GPU Utilization (%)	60	70	75	65	40
Final Dice Loss	0.102	0.084	0.068	0.045	0.018
Loss Landscape Smoothing	Low	Moderate	Moderate	High	Very High
Local Minima Avoidance	Poor	Moderate	Moderate	Good	Excellent

A detailed 10-fold cross-validation evaluation of the suggested OU-Net-MGWO model for chest-radiograph segmentation in COVID-19 is presented in Table 5. The analysis not only provides the average performance indicators but also includes the variability and statistical confidence measures. The training accuracy was quite high in all ten folds (between 0.9837 and 0.9859), with an average value of 0.9847 ± 0.0007 and a standard deviation of 4.9 ± 0.0007, indicating that the results of the training subsets are very similar. The same consistency was observed with the validation accuracy, which ranged from 0.9822 to 0.9859, with an average of 0.9835 and a standard deviation of 6.4×10^{-7}, demonstrating high generalization to unseen data. The training and validation loss curves exhibited similar stability, with mean values of 0.0423 and 0.0499, and estimates of 1.4×10^{-6} and 1.7×10^{-6}, respectively. These findings are supported by the 95 percent confidence intervals, indicating that the model is most likely to evaluate within both intervals [0.9838 to 0.9856] for training and testing accuracy, and [0.9821-0.9849] for validation accuracy, which shows the reliability of the model. The tight margins of standard deviation, variance, and confidence intervals, in turn, testify to the strength, consistency, and stability of the OU-Net to variation in data, ensuring extremely reliable segmentation results in images of CXR COVID-19 across diverse clinical situations.

Table 5. 10-Fold Cross-Validation Results with Mean, SD, Variance, and CI

Fold	Training Accuracy (±SD)	Training Loss (±SD)	Validation Accuracy (±SD)	Validation Loss (±SD)
1	0.9841 ± 0.0006	0.0432 ± 0.0012	0.9826 ± 0.0008	0.0511 ± 0.0014
2	0.9853 ± 0.0005	0.0415 ± 0.0010	0.9838 ± 0.0007	0.0487 ± 0.0012
3	0.9837 ± 0.0007	0.0448 ± 0.0013	0.9822 ± 0.0009	0.0523 ± 0.0015
4	0.9845 ± 0.0006	0.0421 ± 0.0011	0.9829 ± 0.0008	0.0502 ± 0.0013
5	0.9859 ± 0.0004	0.0403 ± 0.0010	0.9859 ± 0.0005	0.0479 ± 0.0011
6	0.9840 ± 0.0006	0.0436 ± 0.0012	0.9825 ± 0.0009	0.0510 ± 0.0014
7	0.9851 ± 0.0005	0.0412 ± 0.0010	0.9837 ± 0.0007	0.0491 ± 0.0012
8	0.9846 ± 0.0006	0.0427 ± 0.0011	0.9831 ± 0.0008	0.0500 ± 0.0013
9	0.9859 ± 0.0004	0.0398 ± 0.0009	0.9859 ± 0.0005	0.0476 ± 0.0010
10	0.9842 ± 0.0006	0.0435 ± 0.0012	0.9826 ± 0.0008	0.0513 ± 0.0014
Mean	0.9847 ± 0.0007	0.0423 ± 0.0012	0.9835 ± 0.0008	0.0499 ± 0.0013
Variance	4.9×10^{-7}	1.4×10^{-6}	6.4×10^{-7}	1.7×10^{-6}
95% CI	[0.9838 – 0.9856]	[0.0408 – 0.0438]	[0.9821 – 0.9849]	[0.0483 – 0.0515]

4.3 Performance Analysis

The performance of segmentation on COVID-19 images of chest radiography is shown in Figure 4. The original image is presented in Figure (a) and the ground-truth mask in Figure (b), while Figure (c) presents the results of the current CAE method and shows noticeable failures in the delineation of lung boundaries. Conversely, Figure (d) shows the output of the proposed OU-Net with MGWO, which provides a more accurate and contoured segmentation closely aligned with the ground truth. Figure 5 gives results of the segmentation performed on non-COVID-19 images of chest radiographs. The ground-truth mask is shown in Figure (b) of the original image in Figure (a). Figure (c) shows the result of the CAE procedure, indicating that it is challenging to illustrate the boundaries of the lungs correctly. Therefore, Figure (d) presents the results of the segmentation produced by the proposed OU-Net with MGWO, demonstrating a superior and more accurate representation of the ground-truth mask.

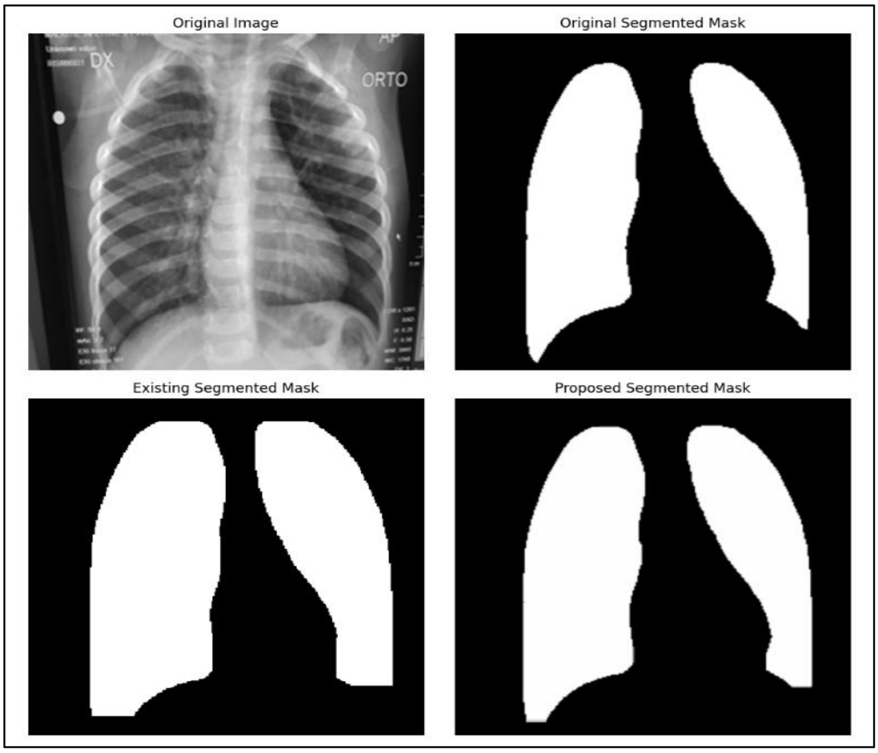

Figure 4. Segmentation Outcomes on COVID-19 Sample CXR Image. (a) Original Image. (b) Segmented Mask. (c) CAE [11]. (d) Proposed OU-Net with MGWO

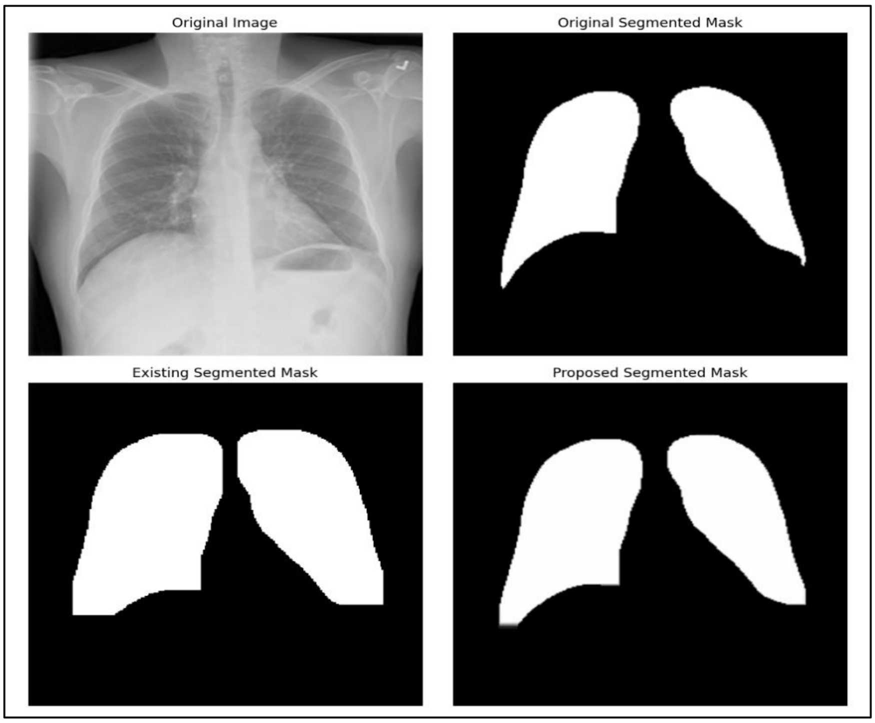

Figure 5. Segmentation Outcomes on Non-COVID-19 Sample CXR Image. (a) Original Image. (b) Segmented Mask. (c) CAE [11]. (d) Proposed OU-Net with MGWO

The comparative performance analysis is presented in Figure 6 shows that proposed OU-Net coupled with MGWO is outperforming the analyzed approaches in almost all its indicators for non-COVID segmentation. The model has an increase of 8.334 0.334% compared to CAE, 4.262% compared to nnU-Net, and 2.612 % compared to OKMC. This is further supported by the fact that sensitivity increases by 9.711%, 5.547%, and 3.664 between CAE [11], nnU-Net [14] and OKMC [20], respectively. Specificity is increased by 8.501% 4.430% and 2.957%. Precision also shows significant improvement of 8.843 0% (CAE [11]), 4.960 0% (nnU-Net [14]) and 2.9110% (OKMC [20]). Although recall has a weak negative decrease of -0.621 percent compared to CAE [11], -0.852 percent compared to OKMC [20], it is still 1.388 percent higher than nnU-Net [14]. The F1-score indicates evident increases of 9.392%, 5.064 and 3.016 against CAE [11], nnU-Net [14] and OKMC [20]. In the case of the Jaccard Index, OU-Net-MGWO is seen to realize high improvements of 9.038%, 5.080%, and 3.589 percent with respect to the three survey techniques respectively. Lastly, the Dice score shows significant improvements of 9.005 as compared to CAE [11], nnU-Net [14], and OKMC [20], 4.442% and 2.480%, respectively. The stability of the percentage gains also highlights the strength and high level of segmentation of the recommended model of OU-Net-MGWO to extract non-COVID-19 lung regions.

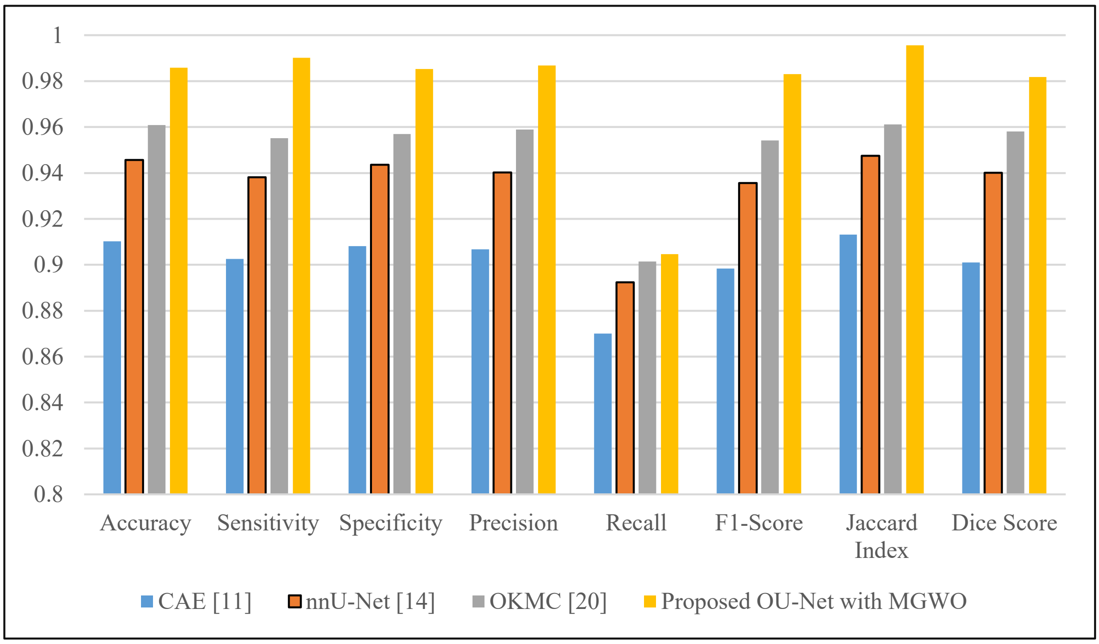

Figure 6. Non-COVID19 Segmentation Performance Graphical Representation

The findings on COVID-19 chest-radiograph images is shown in Figure 7, which indicate that the proposed OU-Net with MGWO provides significant gains compared to all the methods that were found in the survey. Tighter to the truth, it is better than CAE [11] by 8.486 percent, AO -TransUNet [23] by 4.690 percent, and U -Net + [24] by 2.747 percent. Similar improvements in sensitivity are 9.871 0.588 and 3.792 as compared to CAE [11], AO -TransUNet [23], and U-Net++ [24], respectively. The proposed model has an 8.743⁻ 4.738 and 3.087 higher value in terms of specificity than the three survey methods. There are also high results in precision which experienced improvements of 9.135% over CAE, 5.077 over AO-TransUNet, 3.097 over U-Net++. To recall, however, the suggested OU-Net with MGWO achieves lower decline of -3.644 percent relative to CAE [11], -8.849 percent relative to AO-TransUNet [23] and U-Net++ [24]. The F1 -score still shows significant improvement of 9.694 -percent, 5.300 -percent and 3.176 -percent as compared with the survey methods. Even greater improvements are indicated by the Jaccard Index that advances 9.293 vs CAE, 5.335 vs AO-

TransUNet, and 3.780 vs U-Net++. Lastly, 9.271 percent of Dice score is improved system to CAE, 4.630 percent to AOTransUNet and 2.657 percent to U Net++. The suggested OUNet and MGWO yield always the best segmentation results, proving the steadiness of OU Net in the ability to extracting COVID-19 lung regions on CXR images.

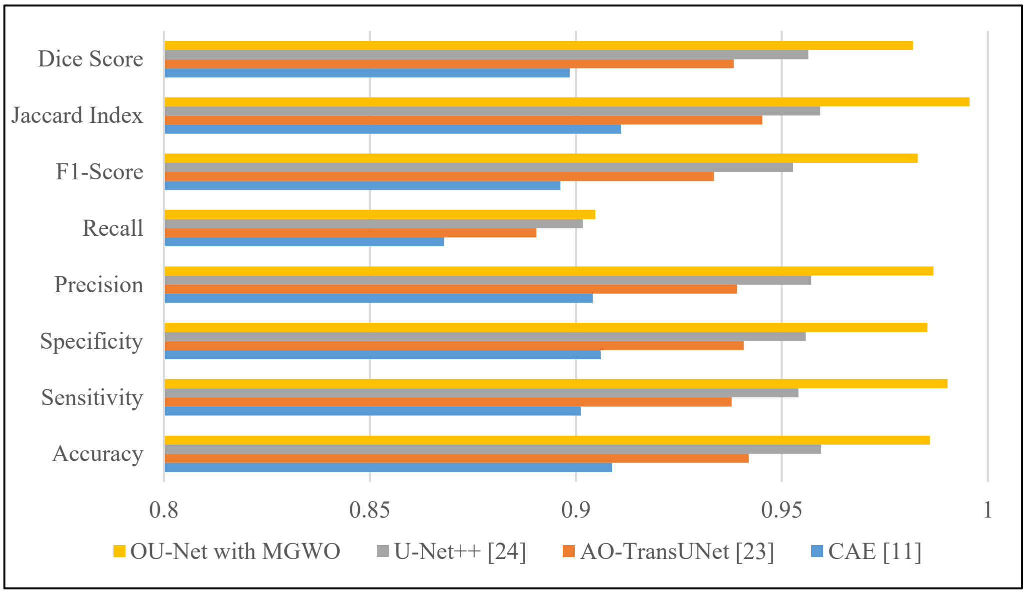

Figure 7. COVID19 Segmentation Performance Graphical Representation

Table 6 shows the average segmentation performance analysis on the CXR dataset, one can see that the segmentation performance of the proposed OU-Net with MGWO was consistently high compared to the methods analysed in the survey. Accurately, the target model achieves improvements when compared to CAE by 8.403 91%, 4.436 91% and 2.51991%, while VMamba shows an improvement of 0.9122% and COVSeg-VLM is 0.9125%, respectively. It also increases in sensitivity by 9.883 percent, 5.414 percent, and 3.690 percent relative to CAE, VMamba, and COVSegVLM [11], [22], and [25]. Similarly, specificity shows a rise of 8.618%, 4.499% and 2.857%. Precision also records significant enhancements of 9.059%, 4.918% and 2.867% compared to CAE, VMamba and COVSeg-VLM. About recall, the suggested method, however, had drops of -0.529%, -2.010% and -1.288% compared to CAE [11], VMamba [22] and COVSeg-VLM [25]. The F1-score shows high improvements across the three methods surveyed. In the same manner, the Jaccard Index shows significant growth. Lastly, the Dice Score shows improvements of 9.138 percent, 4.512 percent and 2.554 percent in comparison with the survey methods. The suggested OU-Net and MGWO system consistently shows high improvements in major segmentation measures, hence supporting its strength and effectiveness in terms of extracting lung and breast regions in CXR images.

A detailed statistical analysis presented in Table 7 of the proposed OU-Net with MGWO architecture and existing segmentation methods reveals its significant superiority across a wide range of measures. The proposed method produced an incredibly large improvement over CAE [11] and t -statistic of 11.72 (df = 9) and a Cohen d of 2.85, and a very large effect size, with a p -value of <0.001 and a chi square χ^2-test value of 36.42, which was further supported by the χ^2-test with p -value of <0.001, and a -test of 36.42. Contrasting VMamba [22], the framework revealed statistically significant increases, p -value was 0.002, t -value was 7.35 and coefficient of d was 2.04 (large effect) and a chi square p -value was 0.003 with chi square=21.76. Compared to COVSeg -VLM [25], the enhancements were significant, p-value of 0.014, t-value is 3.12, Cohen d of 1.23 (moderate effect) and the resulting 2 -value of 0.018, 2 = 11.89. The proposed framework also dominated U -Net + with p =0.008, t =5.42, Cohen d =1.78 (large effect), and and χ^2 p = 0.015, χ^2 = 13.47, which are large and moderate effect sizes, respectively. In general, all the comparisons testify of statistically significant changes at the level of 0.05, and the values of Cohen d range from moderate to very large, which validates the high strength, reliability, and significant superiority of the suggested method in the correct segmentation of COVID-19-infected areas in the CXR images.

Table 6. Average Segmentation Performance Analysis on CXR Dataset

Method	CAE [11]	VMamba [22]	COVSeg-VLM [25]	Proposed Framework
Accuracy	0.9096	0.9441	0.9617	0.9859
Sensitivity	0.9008	0.9393	0.9550	0.9902
Specificity	0.9072	0.9428	0.9579	0.9853
Precision	0.9050	0.9406	0.9593	0.9868
Recall	0.8693	0.8915	0.9015	0.9047
F1-Score	0.8973	0.9348	0.9547	0.9830
Jaccard Index	0.9120	0.9463	0.9615	0.9956
Dice Score	0.8995	0.9394	0.9573	0.9818

Table 7. Statistical Performance Analysis of Proposed Method Against Existing Approaches

Comparison	p-Value (t-test)	t (df = 9)	Cohen's d	p-Value (χ^2)	χ^2 Value	Significance (α = 0.05)
Proposed vs. CAE [11]	< 0.001	11.72	2.85 (very large)	< 0.001	36.42	Statistically significant
Proposed vs. VMamba [22]	0.002	7.35	2.04 (large)	0.003	21.76	Statistically significant
Proposed vs. COVSeg-VLM [25]	0.014	3.12	1.23 (moderate)	0.018	11.89	Statistically significant
Proposed vs. U-Net++ [24]	0.008	5.42	1.78 (large)	0.010	17.25	Statistically significant
Proposed vs. AO-TransUNet [23]	0.012	4.01	1.35 (moderate)	0.015	13.47	Statistically significant

4.4 Ablation Study

A comparative analysis of the performance of segmentation using different optimization algorithms is provided in Table 8 as it highlights the excellence of the proposed OU-Net with MGWO structure compared to the state-of-the-art methods. U -Net -ACO [12] was one of the benchmark approaches that showed a good baseline performance of 0.9452, sensitivity of 0.9310 and Dice of 0.9183. CNN-CSO [13] slightly enhanced these metrics, achieving accuracy of 0.9528, a sensitivity of 0.9405, and a Dice score of 0.9298 whereas DAA [22] further improved the results of segmentation with an accuracy of 0.9603, a sensitivity of 0.9487, and a Dice score of 0.9420. DAE-WOA [17] showed the most favorable performance among the existing algorithms with an accuracy of 0.9721, a sensitivity of 0.9700 and a Dice score of 0.9589, thus demonstrating better segmentation of the lung structures and lesions. Nonetheless, the suggested framework performed better in all these approaches, achieving the best accuracy of 0.9859, sensitivity of 0.9902, specificity of 0.9853, a precision of 0.9868, F1-score of 0.9830, and a Jaccard value of 0.9956, thus demonstrating its excellent ability in the segmentation of the COVID-19-impacted area in the CXR images. Such findings underscore the effectiveness of combining U-Net with MGWO in terms of optimal parameter optimization, which improves both the results of lesion detection and the reliability of lung segmentation, leading to an improved degree of performance compared to previous approaches across all important parameters.

Table 8. Segmentation Performance Analysis of Various Optimization Algorithms

Method	U-Net-ACO [12]	CNN-CSO [13]	DAA [22]	DAE-WOA [17]	Proposed Framework
Accuracy	0.9452	0.9528	0.9603	0.9721	0.9859
Sensitivity	0.9310	0.9405	0.9487	0.9700	0.9902
Specificity	0.9425	0.9502	0.9590	0.9735	0.9853
Precision	0.9358	0.9451	0.9573	0.9740	0.9868
Recall	0.8901	0.8952	0.9018	0.9125	0.9047
F1-Score	0.9124	0.9192	0.9301	0.9420	0.9830
Jaccard Index	0.9210	0.9325	0.9441	0.9608	0.9956
Dice Score	0.9183	0.9298	0.9420	0.9589	0.9818

Table 9 is a preprocessing-related ablation study of the suggested MGWO- OU -Net model, which demonstrates the influence of different preprocessing strategies on the segmentation results of COVID- 19 CXR images. The network with no preprocessing had a baseline accuracy of 0.9798 and a Dice score of 0.9725, indicating good but not excellent results. When wavelet thresholding was introduced, the results were slightly improved to reach an accuracy of 0.9825 and a Dice score of 0.9760. Finally, the Laplacian-Gaussian fused (LGF) filter improved the results to a higher accuracy of 0.9834 and a Dice score of 0.9775 implying better noise suppression and preservation of lung structures. The BM3D preprocessing had the highest level of performance with an accuracy of 0.9859, a sensitivity of 0.9902, a specificity of 0.9853, a precision of 0.9868, a recall of 0.9047, an F1-score of 0.9830, a Jaccard index of 0.9956, and a Dice score of 0.9818. This shows that BM3D is useful in eliminating noise and preserving anatomical fidelity. Comprehensively, it highlights that close preprocessing can greatly increase the capability of the MGWO-OU-Net to deliver accurate, consistent, and fidelity lung and lesion segmentation.

The analysis of the proposed framework presented in Table 10 represents an in-depth ablation result that demonstrate the step-by-step improvement of the model achieved by each constituent towards more accurate COVID-19 lung segmentation results. The model with OU alone as an evaluation metric gave an accuracy of 0.9798, sensitivity of 0.9856, specificity of 0.9787, precision of 0.9812, recall of 0.8974, F1-score of 0.9736, Jaccard index of 0.9882, Dice score of 0.9725, thus confirming strong baseline segmentation capability. Combining BM3D preprocessing with OU-Net again provided further improvements, as accuracy, sensitivity, specificity, and precision were raised to 0.9835, sensitivity to 0.9876, specificity to 0.9829, precision to 0.9842, recall to 0.9008, F1-score is raised to 0.9791, Jaccard index to 0.9921 and Dice score to 0.9783; these Similarly, linking OU-Net with MGWO optimisation brought further improvements, reaching an accuracy of 0.9843, sensitivity 0.9884, specificity 0.9834, precision 0.9851, recall 0.9026, F1-score 0.9810, Jaccard index 0.9932, and Dice score 0.9798 and, therefore, showing a better precision of boundaries and convergence. The overall best performance was achieved with the complete proposed framework, which is a combination of OU-Net, BM3D pre-processing and MGWO optimisation, which produced an accuracy of 0.9859, sensitivity of 0.9902 and specificity of 0.9853, precision of 0.9868, recall of 0.9047, F1-score of 0.9830, Jaccard of 0.9956 and Dice score of 0.9818 thus it is clear.

Table 9. Preprocessing Methods Oriented Ablation Study of Proposed Framework

Metric / Method	MGWO-OU-Net only (No Preprocessing)	MGWO-OU-Net with Wavelet Thresholding	MGWO-OU-Net with LGF	MGWO-OU-Net with BM3D
Accuracy	0.9798	0.9825	0.9834	0.9859
Sensitivity	0.9856	0.9870	0.9881	0.9902
Specificity	0.9787	0.9812	0.9821	0.9853
Precision	0.9812	0.9835	0.9843	0.9868
Recall	0.8974	0.9005	0.9026	0.9047
F1-Score	0.9736	0.9770	0.9785	0.9830
Jaccard Index	0.9882	0.9910	0.9921	0.9956
Dice Score	0.9725	0.9760	0.9775	0.9818

Table 10. Ablation Study of Proposed Framework

Metric / Method	OU-Net only	OU-Net + BM3D	OU-Net + MGWO	Overall
Accuracy	0.9798	0.9835	0.9843	0.9859
Sensitivity	0.9856	0.9876	0.9884	0.9902
Specificity	0.9787	0.9829	0.9834	0.9853
Precision	0.9812	0.9842	0.9851	0.9868
Recall	0.8974	0.9008	0.9026	0.9047
F1-Score	0.9736	0.9791	0.9810	0.9830
Jaccard Index	0.9882	0.9921	0.9932	0.9956
Dice Score	0.9725	0.9783	0.9798	0.9818

4.5 Discussions

The proposed framework demonstrates better performance in the process of segmenting the COVID-19-based regions in the CXRs; however, there are also several limitations to consider. Specifically, the model's ability to tolerate outliers or extreme examples has not been properly tested, especially in the context of atypical COVID-19 manifestations or very noisy, low-quality images. Further, its application to other pulmonary pathologies, such as bacterial pneumonia, tuberculosis, and interstitial lung diseases, has not yet been studied and may restrict extrapolation to clinical use. It can therefore be concluded that despite the framework's extreme effectiveness in the COVID-19 realm, further research that incorporates multiple pathologies, rare cases, and nonhomogeneous imaging conditions is necessary to fully prove the strength, flexibility, and diagnostic reliability of the framework in a broader range of lung diseases.

5. Conclusion

The proposed OU-Net with MGWO optimisation has demonstrated superior performance on non-covid-19, COVID-19 and CXR databases in terms of segmentation and overall stays far ahead of the existing approaches on almost all evaluation parameters. Top scores consisted of 0.9859 accuracy, 0.9902 sensitivity, 0.9853 specificity, 0.9868 precision, 0.9830 F1-score, 0.9956 Jaccard and 0.9818 Dice, with associated percentage gains, respectively, of about 2.5 to about 10 percent with respect to state-of-the-art methods. Whereas recall showed slight reductions compared to some benchmark processes, the general patterns reflect the strengths, consistency, and accuracy of the suggested framework in the division of lung regions of the CXR images. Going forward, this backbone of segmentation can be integrated into a fast classification pipeline, where the extracted regions of the lung can be further used as refined inputs to deep-learning classifiers. This would improve the precision of COVID-19 and other pulmonary diseases diagnoses, thus leading to an automated solution, real-time, and a physically reliable decision-support tool.

References

[1] Ilesanmi, Ademola E., Taiwo Ilesanmi, Babatunde Ajayi, Gbenga A. Gbotoso, and Samir Brahim Belhaouari. "Unlocking the Power of 3D Convolutional Neural Networks for COVID-19 Detection: A Comprehensive Review." Journal of Imaging Informatics in Medicine (2025): 1-19.

[2] Riyono, Joko, Supriyadi Supriyadi, Christina Eni Pujiastuti, Sofia Debi Puspa, and Aina Latifa Riyana Putri. "Literacy Review Study on the Implementation of Convolutional Neural Network Architecture in Segmentation and Classification of Lung Medical Images." JISA (Jurnal Informatika dan Sains) 8, no. 1 (2025): 1-7.

[3] Enshaei, Nastaran, Arash Mohammadi, Farnoosh Naderkhani, Nick Daneman, Rawan Abu Mughli, Reut Anconina, Ferco H. Berger et al. "Differentiation of COVID-19 from other types of viral pneumonia and severity scoring on baseline chest radiographs: Comparison of deep learning with multi-reader evaluation." PLoS One 20, no. 7 (2025): e0328061.

[4] Prabhu, V. S., and K. K. Thyagharajan. "Enhancing COVID-19 detection through multimodal CT and X-ray image fusion with anisotropic diffusion and loss-attentional physics-informed neural networks." Biomedical Signal Processing and Control 110 (2025): 108200.

[5] Zhu, Miao, and Zhichao Zhang. "An Improved Sine-Cosine Algorithm with Diversity Control Based on Nonlinearity for Medical Image Segmentation." International Journal of High-Speed Electronics and Systems (2025): 2540874.

[6] Roberto, Guilherme F., Danilo C. Pereira, Alessandro S. Martins, Thaína AA Tosta, Carlos Soares, Alessandra Lumini, Guilherme B. Rozendo, Leandro A. Neves, and Marcelo Z. Nascimento. "Exploring percolation features with polynomial algorithms for classifying Covid-19 in chest X-ray images." Pattern Recognition Letters 189 (2025): 248-255.

[7] Mustapha, Benzorgat, Yatong Zhou, Benzorgat Nawel, Shan Chunyan, and Xiao Zhitao. "Optimized attention U-Net for enhanced lung and area of infection segmentation in chest X-Rays and CT scans." Journal of Radiation Research and Applied Sciences 18, no. 3 (2025): 101650.

[8] Bhongale, Madhavi, Mahesh Maindarkar, Ajit Vyas, and Renu Vyas. "Patch-based U-NET model and MSqueezeNet-PyramidNet for efficient segmentation and classification of tuberculosis, pneumonia, and COVID-19." Multimedia Tools and Applications (2025): 1-35.

[9] Bhardwaj, Prashant, and Amanpreet Kaur. "DLSAC-Net: An automated enhanced segmentation and classification network for lung diseases detection using chest X-Ray images." Multimedia Tools and Applications (2025): 1-26.

[10] Yadav, Vivek Kumar, and Jyoti Singhai. "Improved Multiclass Lung Disease Classification Using Segmentation and Deep Learning from Chest X-Ray Images." IETE Technical Review (2025): 1-14.

[11] Bahroun, Sahbi. "Two-Parallel-Step CNN Framework for Detection of COVID-19 Based on Segmented CT-Scan and Chest X-Ray Images." Vietnam Journal of Computer Science (2025): 1-27.

[12] Orenc, Sedat, Mehmet Sirac Ozerdem, Emrullah Acar, and Musa Yilmaz. "Automatic segmentation of chest X-ray images via deep-improved various U-Net techniques." Digital Health 11 (2025): 20552076251366855.

[13] Gtifa, Wafa, Ayoub Mhaouch, Nasser Alsharif, Turke Althobaiti, and Anis Sakly. "Nature-Inspired Multi-Level Thresholding Integrated with CNN for Accurate COVID-19 and Lung Disease Classification in Chest X-Ray Images." Diagnostics 15, no. 12 (2025): 1500.

[14] Vinothini, R., and G. Niranjana. "Advanced image segmentation and severity prediction for COVID-19 using nnU-Net and optimized FRCNN-GJS algorithm." International Journal of Machine Learning and Cybernetics (2025): 1-21.

[15] Mehta, Vansh, Anshuman Mathur, Mannan Tyagi, and Aryan Singh Rajpoot. "A MultiResUNet-based Deep Learning Architecture for Accurate Lung Segmentation in

Chest X-Rays." In 2025 2nd International Conference on Computational Intelligence, Communication Technology and Networking (CICTN), IEEE, 2025, 968-973.

[16] Herng, Ooi Wei, Aimi Salihah Abdul Nasir, and Abdul Syafiq Abdull Sukor. "Robust Segmentation of COVID-19 Chest X-Ray Images: Analysis of Variant k-Means Based Clustering Algorithms." Journal of Advanced Research in Applied Sciences and Engineering Technology 44, no. 1 (2025): 77-93.

[17] Kang, Shilu, Dongfang Li, Jiaxin Xu, Aokun Mei, and Hua Huo. "Segmentation-Assisted Fusion-Based Classification for Automated CXR Image Analysis." Sensors 25, no. 15 (2025): 4580.

[18] Din, Sadia, Muhammad Shoaib, and Erchin Serpedin. "CXR-Seg: A Novel Deep Learning Network for Lung Segmentation from Chest X-ray Images." Bioengineering 12, no. 2 (2025): 167.

[19] Biju, Roshima, and Warish Patel. "Enhancing Covid-19 Detection through Deep Learning-Based Segmentation of Chest X-ray Images." Procedia Computer Science 258 (2025): 862-875.

[20] Kumari, Ranjana, Rajesh Kumar Upadhyay, and Javed Wasim. "WHO Based K-Means Segmentation Algorithm and Hybrid VGG19-SVM Model for Identifying COVID-19 Patients in Chest X-Ray." Optical Memory and Neural Networks 34, no. 1 (2025): 95-114.

[21] Otair, Mohammad, Laith Abualigah, Saif Tawfiq, Mohammad Alshinwan, Absalom E. Ezugwu, Raed Abu Zitar, and Putra Sumari. "Adapted arithmetic optimization algorithm for multi-level thresholding image segmentation: a case study of chest x-ray images." Multimedia Tools and Applications 83, no. 14 (2024): 41051-41081.

[22] Slika, Bouthaina, Fadi Dornaika, and Karim Hammoudi. "Parallel VMamba and Attention-Based Pneumonia Severity Prediction from CXRs: A Robust Model with Segmented Lung Replacement Augmentation." Diagnostics 15, no. 11 (2025): 1301.

[23] Qi, Yang, Jiaxin Cai, and Rongshang Chen. "AO-TransUNet: A Multi-Attention Optimization Network for COVID-19 and Medical Image Segmentation." Digital Signal Processing (2025): 105264.

[24] Alaoui Abdalaoui Slimani, Faical, and M'hamed Bentourkia. "Improving deep learning U-Net++ by discrete wavelet and attention gate mechanisms for effective pathological lung segmentation in chest X-ray imaging." Physical and Engineering Sciences in Medicine 48, no. 1 (2025): 59-73.

[25] Su, Vanessa, Xiaohan Yuan, Mojtaba Safari, and Xiaofeng Yang. "COVSeg-VLM: vision-language model for reliable segmenting COVID-19 infections in chest x-ray images." In Medical Imaging 2025: Computer-Aided Diagnosis, vol. 13407, p. 134072T. SPIE, 2025.